processes

MDPI

Article

Study on the Influence of Inlet Inclination Angle on the Erosion Characteristics of a Drilling Float Valve

Xin Zhang [1], Junan Lu [1], Yanwen Liu [1,*], Xitian Shi [1], Xuliang Zhang [1] and Lin Zhong [2,*]

[1] Petrochina Tarim Oilfield Company, Korla 841000, China
[2] College of Mechanical Engineering, Southwest Petroleum University, Chengdu 610500, China
* Correspondence: liuyw-tlm@petrochina.com.cn (Y.L.); zhonglin858296@163.com (L.Z.)

Abstract

Localized erosion near the valve cover and pin shaft can impair the reliability of drilling float valve. This study investigates an eccentric contraction modification for a 62 mm float valve, in which the small-end cross-section is shifted away from the pin shaft while the diameters of both end sections remain unchanged. Computational fluid dynamics simulations incorporating the RNG k–ε turbulence model, discrete phase model, and Oka erosion model were conducted to investigate the erosion characteristics for inlet inclination angles of 4.5–8.5°. At a flow rate of 20 L/s, a solid volume fraction of 0.5%, and a drilling-fluid viscosity of 20 mPa·s, increasing the inclination angle from 4.5° to 8.5° reduced the average erosion rates of the valve cover and valve spool body by 94% and 51%, respectively. The modification redirected particle-laden flow away from these critical components and reduced concentrated particle impacts. The effects of particle size, fluid viscosity, and solid concentration were also examined. Comparative tests conducted for 15 h at 20 L/s and a sand volume fraction of 15% showed visibly less valve-cover damage for the structural optimization of float valve, providing qualitative support for the predicted improvement. An inclination angle of 8.5° is recommended within the investigated geometric and seal-installation constraints.

Keywords: drilling float valve; inlet inclination angle; erosion characteristics; structural optimization

1. Introduction

With economic and social development, national demand for energy continues to increase. The 15th Five-Year Plan identifies deep and ultra-deep oil and gas exploration and development as strategic measures for ensuring energy security. The Tarim Oilfield is a major area for deep and ultra-deep well (4500–9000 m) exploration and development in China [1,2]. By the end of 2025, more than 250 ultra-deep wells with depths exceeding 8000 m had been drilled in this field, accounting for more than half of China's total. This field has become China's largest ultra-deep oil and gas production base [3]. The formations in the Tarim Oilfield are extremely complex, with high bottomhole temperature, high pressure, and high H_2S concentrations, making the field a difficult area for deep and complex oil and gas drilling worldwide [4,5]. As exploration and development extend to ultra-deep and extra-deep layers, the "three-high and one-super" conditions (high temperature, high pressure, high H_2S concentration, and ultra-deep reservoirs) have become increasingly common, and well control risks have increased. Inner blowout prevention tools are critical

Check for updates

Academic Editor: Marco Ramírez-Argáez

Received: 8 October 2026
Revised: 1 November 2026
Accepted: 4 November 2026
Published: 6 November 2026

Copyright: © 2026 by the authors. Licensee MDPI, Basel, Switzerland. This article is an open access article distributed under the terms and conditions of the Creative Commons Attribution (CC BY) license.

equipment for ensuring drilling well control safety and play a vital role in deep and ultra-deep drilling operations [6].

The drilling float valve is an inside-drill-string blowout preventer that maintains one-way flow of drilling fluid and prevents blowout or backflow during kicks or well surges. According to their structural form, float valves are divided into arrow-type (F-type) and flapper-type (G-type) valves [7]. The flapper-type float valve (hereinafter referred to as the float valve) is more widely used in the Tarim Oilfield. Because the float valve is installed near the bit downhole, it can isolate high-pressure oil and gas at the moment of a kick or blowout, thereby preventing well control accidents [8]. Statistics from the Emergency Center of Tarim Oilfield Company show that 3226 float valve spools were recovered in 2024, of which 1377 (42.68%) were abnormally damaged. The average service life of these spools was approximately 100–200 h. Among the damaged spools, spring failure accounted for 51%, rubber seal failure for 44%, valve cover detachment for 4%, and other causes for 1%. Further analysis showed that the valve cover, spool body, pin shaft, and torsion spring exhibited varying degrees of erosion. This damage was mainly caused by solid particles in the high-pressure, high-speed drilling fluid repeatedly scouring and eroding the float valve components, resulting in rapid failure. Chen et al. [9] discussed the working mechanisms and erosion-related failure of drill-string check valves. Zhang et al. [10] applied CFD to analyze the flow field in a flapper-type float valve. Xu et al. [11] compared simulated flow patterns with observed erosion and proposed structural modifications that reduced vortices and high-velocity regions.

Recent CFD studies have linked erosion reduction to flow-path design and particle impact conditions. Tang et al. [12] identified the sliding-core inlet angle and particle size as major factors in erosion of a pressure-controlled injection tool. Zhang et al. [13] reduced bypass-valve erosion by modifying the side-hole number and flow-channel cone angle. Zhao et al. [14] used CFD-DPM to relate needle-throttle-valve erosion to valve opening and particle transport in gas–solid flow. These studies support geometry-based erosion mitigation, but their optimized parameters depend on the valve geometry and carrier phase; they do not establish the allowable eccentric contraction for a liquid–solid float valve. Related modeling approaches address other aspects of drilling-system reliability. Wang et al. [15] developed a decoupling model for fatigue-life assessment of a double wellhead system with a subsea suction anchor, while Wang et al. [16] combined multiphase heat-transfer modeling and inverse design for phase-change-assisted wellbore cooling. These studies highlight the need to link mechanism-specific predictions to the corresponding operating conditions and design constraints.

This study therefore investigates a float valve spool with a diameter of 62 mm and optimizes its internal flow field. Different inlet inclination angles are evaluated to determine their effects on the flow-field distribution. The objective is to reduce erosion of vulnerable components such as the torsion spring and pin shaft by the circulating drilling fluid and to provide a theoretical basis for the structural optimization of float valves.

2. Materials and Methods

2.1. Float Valve Structure and Working Principle

The float valve spool consists of an annular rubber seal, valve seat, torsion spring, pin shaft, shock-absorbing rubber ring, end-face rubber seal, valve cover, and spool body, as shown in Figure 1. The float valve is installed inside the drill string near the bit. It consists of the float valve spool assembly and the float valve body, which is connected to the drill string [10] (Figure 2). During normal drilling circulation, the drilling fluid pushes the valve cover open and establishes the flow passage. If the formation pressure exceeds the pressure inside the drill string, it pushes the drilling fluid upward and may cause a kick or blowout.

Once circulation stops or a kick or blowout occurs downhole, the torsion spring rapidly closes the valve cover, sealing the bottomhole flow passage and preventing blowout [10,11].

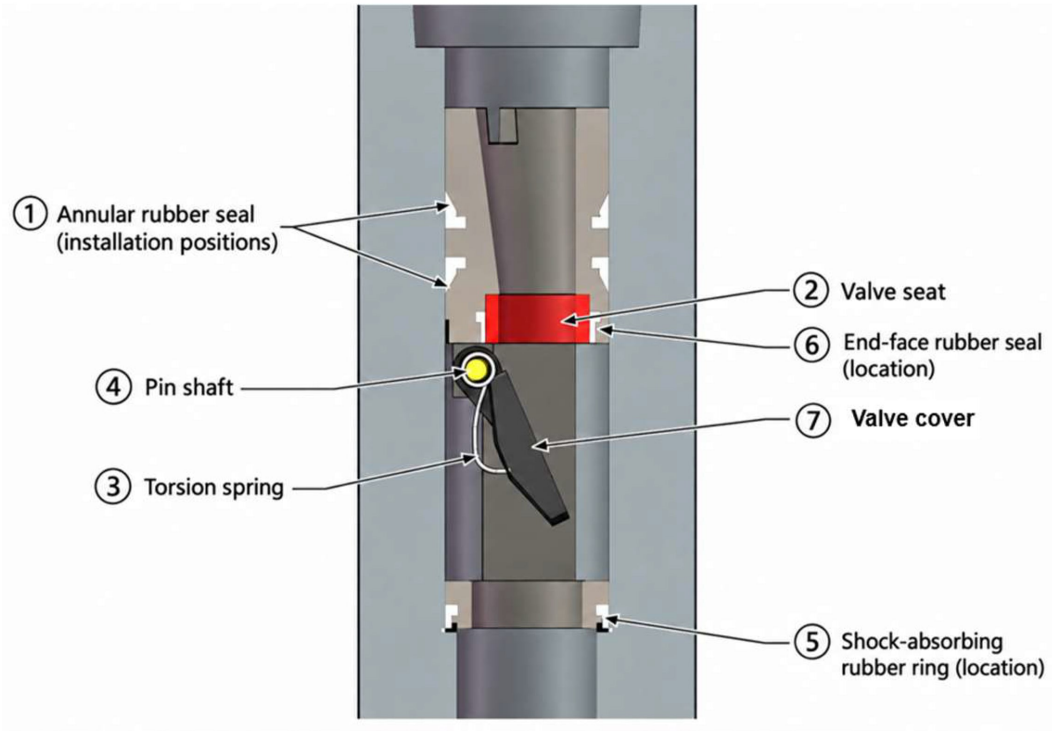


Figure 1. Sectional view of the float valve.

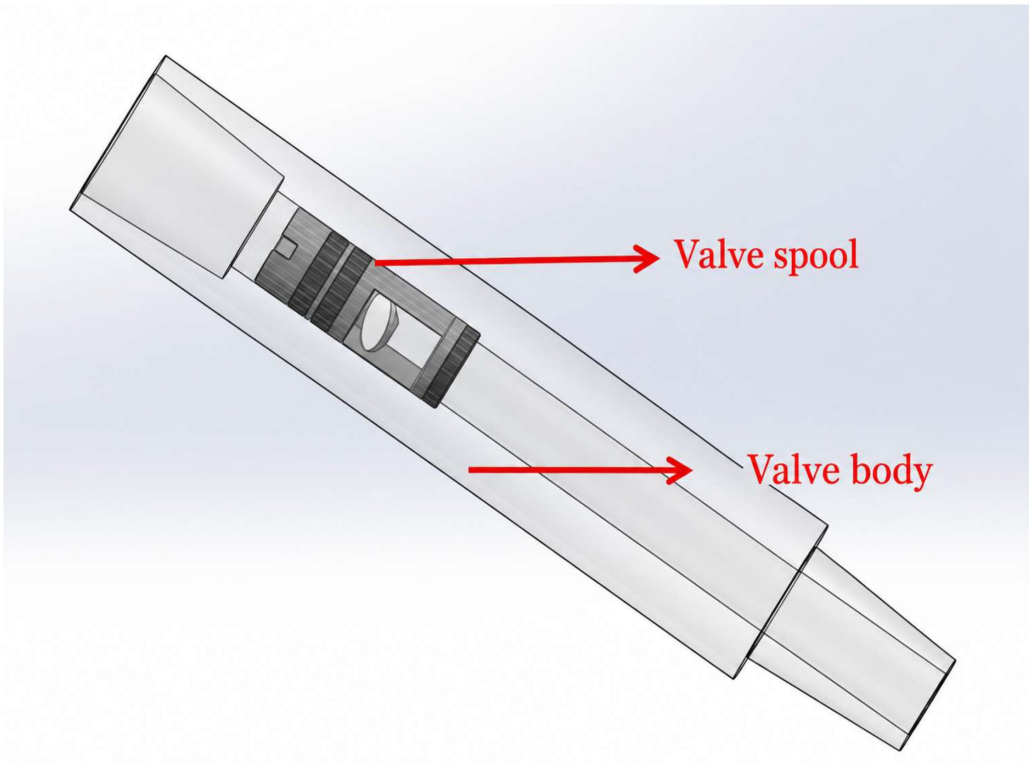


Figure 2. Installation schematic of the float valve.

2.2. Geometric Model

The modeling workflow is shown in Figure 3. To ensure simulation accuracy, a three-dimensional model of a 62 mm float valve was constructed based on the actual dimensions.

The chamfers and small steps were reasonably simplified to reduce computational cost and improve mesh quality. The model was then imported into Spaceclaim, and the internal fluid domain of the float valve was extracted. Finally, the fluid domain was meshed in Fluent Meshing. The inlet contraction was modified by changing the outlet offset, as illustrated in Figure 4.

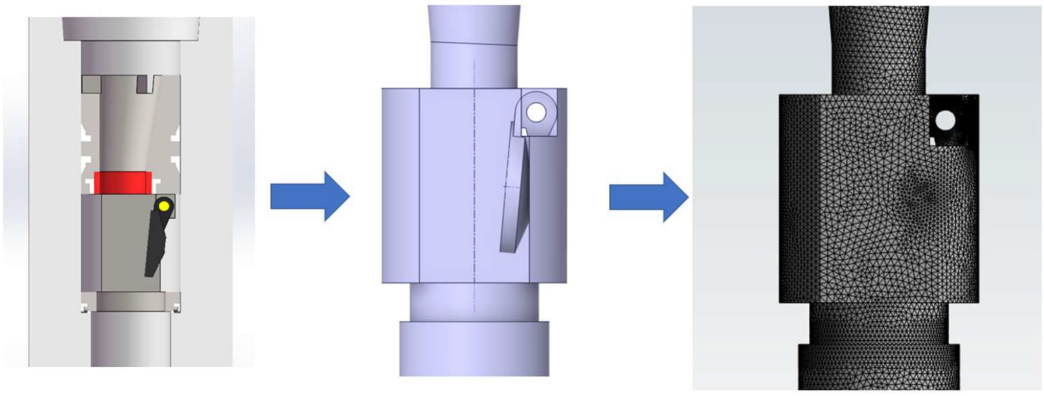


Figure 3. Modeling process for the float valve.

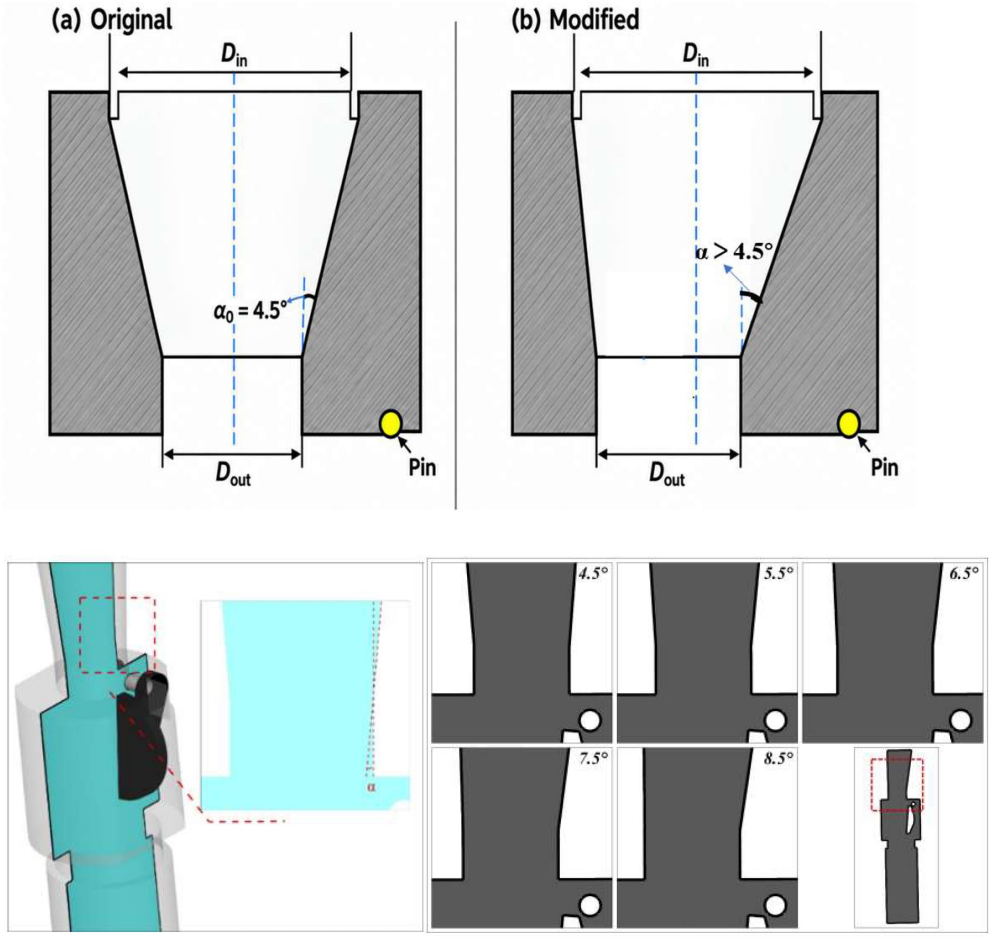


Figure 4. Definition and geometric variation in the inlet inclination angle. Upper: (**a**) original concentric contraction and (**b**) modified eccentric contraction (schematic, not to scale). Lower: geometric models with inlet inclination angles of 4.5°, 5.5°, 6.5°, 7.5°, and 8.5°.

The inlet inclination angle α is defined in the longitudinal section along the direction of eccentricity as the acute angle between the contraction wall on the pin-shaft side and

a line parallel to the main-channel axis. The large- and small-end cross-sections of this internal contraction retain their respective diameters, labeled D_{in} and D_{out} in Figure 4. These local sections are distinct from the inlet and outlet boundaries of the computational domain. In the original 62 mm float valve, the two sections are coaxial and $\alpha = 4.5°$. The modified configurations shift the small-end section away from the pin shaft while keeping the large-end section fixed. Increasing the offset e between the two section centers increases α. Five configurations with $\alpha = 4.5°$, 5.5°, 6.5°, 7.5°, and 8.5° were constructed.

The investigated range is determined by the original geometry and the space available for installing the rubber seal. For the present valve dimensions and seal arrangement, 8.5° corresponds to the maximum lateral offset of the small-end section that permits normal seal installation. A further increase in offset would interfere with seal installation and compromise the sealing function. Thus, angles above 8.5° lie outside the feasible range of the present design.

2.3. Mathematical Models

The internal flow field of the float valve is a typical solid–liquid two-phase turbulent flow, in which quantities such as velocity and pressure fluctuate randomly in space and time. Time averaging is applied with a turbulence model to close the model equations and establish relationships for the turbulent fluctuation terms [17,18]. The RNG k-ε turbulence model was adopted, and the Reynolds stress was related to the turbulent kinetic energy and turbulent dissipation rate through the eddy viscosity hypothesis. The RNG k–ε model was selected because its strain-dependent correction in the ε equation improves its response to rapid strain and streamline curvature, making it suitable for the accelerating and turning flow within the float valve.

2.3.1. Governing Equations

Assuming incompressible, isothermal flow and applying time averaging, the Reynolds-averaged Navier–Stokes equations are obtained as follows.

Mass conservation equation:

$$\frac{\partial \rho}{\partial t} + \frac{\partial}{\partial x_i}(\rho u_i) = 0 \tag{1}$$

Momentum conservation equation:

$$\frac{\partial(\rho \mathrm{u_i})}{\partial \mathrm{t}} + \frac{\partial(\rho \mathrm{u_i u_j})}{\partial \mathrm{x_j}} = \frac{\partial \mathrm{p}}{\partial \mathrm{x_i}} + \frac{\partial}{\partial \mathrm{x_j}}\left[\mu\left(\frac{\partial \mathrm{u_i}}{\partial \mathrm{x_j}} + \frac{\partial \mathrm{u_j}}{\partial \mathrm{x_i}} - \frac{2}{3}\delta_{\mathrm{ij}}\frac{\partial \mathrm{u_k}}{\partial \mathrm{x_k}}\right)\right] + \frac{\partial}{\partial \mathrm{x_j}}\left(-\rho\overline{\mathrm{u_i' u_j'}}\right) \tag{2}$$

where $\mathrm{u_i}$ is the time-averaged velocity. When $\mathrm{i = j}$, $\delta_{\mathrm{ij}} = 1$; when $\mathrm{i \neq j}$, $\delta_{\mathrm{ij}} = 0$.

2.3.2. Turbulent Transport Equations

The RNG k-ε turbulence model provides reliable performance, rapid convergence, high accuracy, and low memory requirements in simulations [18].

Turbulent kinetic energy k equation:

$$\frac{\partial(\rho \mathrm{k})}{\partial \mathrm{t}} + \frac{\partial(\rho \mathrm{k u_i})}{\partial \mathrm{x_i}} = \frac{\partial}{\partial \mathrm{x_j}}\left[\left(\mu + \frac{\mu_{\mathrm{i}}}{\sigma_{\mathrm{k}}}\right)\frac{\partial \mathrm{k}}{\partial \mathrm{x_j}}\right] + \mathrm{G_k} + \mathrm{G_b} - \rho\varepsilon - \mathrm{Y_M} + \mathrm{S_k} \tag{3}$$

Dissipation rate ε equation:

$$\frac{\partial(\rho\varepsilon)}{\partial t} + \frac{\partial(\rho k u_i)}{\partial x_i} = \frac{\partial}{\partial x_j}\left[\left(\mu + \frac{\mu_t}{\sigma_k}\right)\frac{\partial k}{\partial x_j}\right] + C_{1\varepsilon}\frac{\varepsilon}{k}(G_k + C_{3\varepsilon}G_h) - C_{2\varepsilon}\rho\frac{\varepsilon}{k} + S_c \tag{4}$$

where $\mathrm{G_k}$ is the generation of turbulent kinetic energy due to mean velocity gradients; $\mathrm{G_b}$ is the generation due to buoyancy; $\mathrm{Y_M}$ is the contribution of fluctuating dilatation in compressible turbulence to the overall dissipation rate; $\mathrm{S_k}$ is the user-defined source term for turbulent kinetic energy; $\mathrm{S_c}$ is the user-defined source term for dissipation rate.

2.3.3. Erosion Model

The Oka erosion model [19] was selected because it accounts for particle impact velocity, impact angle, particle diameter, and target-material hardness. These factors are relevant to the present study, which considers sand particles with diameters of 0.106–1.08 mm impacting 35CrMo steel surfaces. The wall hardness of approximately 2.9 GPa was incorporated into the model. For the liquid–solid drilling-fluid flow, particle trajectories and local impact conditions were obtained using the DPM, with fluid viscosity influencing particle transport through the fluid–particle interaction forces. The Oka model then relates these impact conditions to material removal, providing a basis for comparing erosion distributions and trends among different inclination angles. Since the model is empirical, quantitative prediction of absolute erosion rates requires validation under matching fluid, particle, and wall-material conditions. The model is expressed as:

$$ER = 1 \times 10^{-9} K \rho_p f(\alpha) (Hv)^{k_1} \left(\frac{v_p}{V'}\right)^{k_2} \left(\frac{d_p}{d'}\right)^{k_3} \quad (5)$$

$$f(\theta) = (\sin\theta)^{n_1} [1 + Hv(1 - \sin\theta)]^{n_2} \quad (6)$$

$$n_1 = 0.71(Hv)^{0.14} \quad n_2 = 2.4(Hv)^{-0.94} \quad k_2 = 2.3(Hv)^{0.038} \quad (7)$$

where E_{mass} is the erosion rate expressed as the mass loss rate; H_v is the Vickers hardness; E_{ref} is the reference erosion rate; D_{ref} is the reference particle erosion depth; $g(\theta)$ is the impact angle function; f_s is the particle property factor; k_1 and k_2 are empirical constants; n_1, n_2 and n_3 are hardness exponent functions.

2.3.4. Discrete Phase Model and Particle-Wall Rebound

The simulations were performed in Ansys Fluent 2024 R1 using an Eulerian-Lagrangian discrete phase model (DPM). The drilling fluid was solved as the continuous phase using the RANS equations and RNG k-ε turbulence model, while sand particles were tracked in a Lagrangian frame. Particles were introduced by surface injection at the computational inlet. Fluent's spherical drag law was used, and the discrete random walk model was enabled to represent turbulent dispersion. Particle motion follows the force balance below, with the hydrodynamic drag expressed explicitly:

$$m_p \frac{d\boldsymbol{u}_p}{dt} = \sum \boldsymbol{F}_p, \quad \boldsymbol{F}_D = \frac{1}{2} C_D \rho A_p \left|\boldsymbol{u} - \boldsymbol{u}_p\right| \left(\boldsymbol{u} - \boldsymbol{u}_p\right) \quad (8)$$

Here, m_p and u_p are the particle mass and velocity, ΣF_p is the resultant force on the particle, F_D is the drag force, ρ and u are the fluid density and local velocity used for particle tracking, and $A_p = \pi {d_p}^2/4$ is the projected area of a spherical particle. The drag coefficient C_D is evaluated using the spherical drag law. The random walk model includes turbulent velocity fluctuations in particle tracking. The resulting wall-impact velocities and angles are supplied to the Oka erosion model.

Particle rebound at the erosion-evaluated steel walls was described using normal and tangential restitution coefficients following Tang et al. [12]. The coefficients relate the magnitudes of the corresponding particle velocity components after and before impact:

$$e_n = 0.993 - 0.0307\theta_p + 4.75 \times 10^{-4}\,\theta_p^2 - 2.61 \times 10^{-6}\,\theta_p^3 \quad (9)$$

$$e_t = 0.988 - 0.029\theta_p + 6.43 \times 10^{-4}\,\theta_p^2 - 3.56 \times 10^{-6}\,\theta_p^3 \quad (10)$$

Here, e_n and e_t are the normal and tangential restitution coefficients, respectively. θ_p is the particle impact angle measured from the local wall surface, expressed in degrees (0° for grazing impact and 90° for normal impact), and is distinct from the geometric inlet inclination angle α. After impact, the normal velocity component reverses direction and is scaled by e_n, while the tangential component is scaled by e_t.

2.4. Boundary Conditions

A velocity inlet boundary condition was applied, with an inlet velocity of 16.74 m/s (corresponding to a drilling fluid flow rate of 20 L/s) and a turbulence intensity of 5%. A pressure outlet boundary condition was specified at 70 MPa based on field investigations, which identified this value as a commonly encountered downhole operating pressure for the 62 mm float valve. This setting was adopted to represent typical downhole pressure conditions for the investigated valve size. A no-slip condition was imposed on the walls, and standard wall functions were used for near-wall treatment. The governing equations were discretized using the finite volume method, and a high-order upwind scheme was used for the convective terms [10].

The liquid–solid two-phase flow in the float valve must be solved accurately in Fluent, and the erosion of the float valve spool is evaluated using the erosion model. The continuous phase is drilling fluid with a density of 1200 kg/m^3 and a viscosity of 20 mPa·s; the sand particles have a density of 2700 kg/m^3. The spool is made of quenched and tempered 35CrMo steel with a Brinell hardness of approximately 285 HBW (about 295–300 HV), which corresponds to an indentation hardness of approximately 2.9 GPa. This value is used as the material hardness parameter in the Oka erosion model.

Iterative convergence was assessed using both residual reduction and the stability of the monitored erosion rate. The convergence criteria were residuals below 0.001 and a stable monitored erosion rate as the calculation continued.

2.5. Mesh Generation and Sensitivity Assessment

The internal fluid domain was discretized using a tetrahedral mesh in Fluent Meshing, as shown in Figure 3. The mesh was refined in the spool region to improve resolution of local flow gradients. Three boundary-layer mesh layers were generated adjacent to the solid walls. The minimum orthogonal quality was above 0.2. Standard wall functions were used with the RNG k-ε model, as specified in Section 2.4.

Six meshes containing 35,825; 40,871; 86,816; 125,586; 248,397; and 500,409 cells were compared under the same solver settings. Figure 5 and Table 1 summarize the average and maximum erosion rates. Increasing the cell count from 248,397 to 500,409 changed the average and maximum erosion rates by approximately 1.1% and 6.9%, respectively, relative to the finer mesh. The 248,397-cell mesh was selected to balance computational cost and sensitivity of the erosion results.

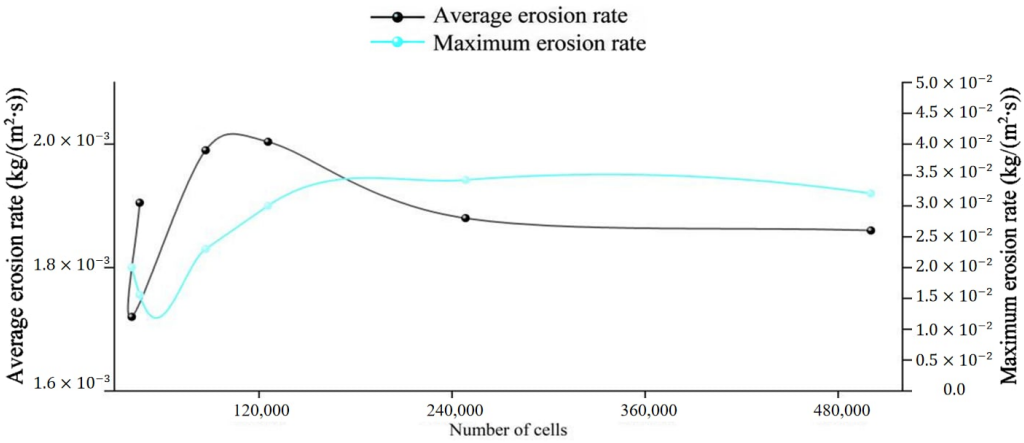


Figure 5. Mesh sensitivity of the average and maximum erosion rates.

Table 1. Average and maximum erosion rates and relative differences between successive meshes.

Number of Cells	Average Erosion Rate ($\times 10^{-3}$ kg·m^{-2}·s^{-1})	Maximum Erosion Rate ($\times 10^{-2}$ kg·m^{-2}·s^{-1})	Relative Difference in Average Erosion Rate (%)	Relative Difference in Maximum Erosion Rate (%)
35,825	1.72	2.00	9.9	29.0
40,871	1.91	1.55	4.0	32.6
86,816	1.99	2.30	0.5	23.3
125,586	2.00	3.00	6.4	12.3
248,397	1.88	3.42	1.1	6.9
500,409	1.86	3.20	—	—

2.6. Model Validation

An erosion test was conducted using the recirculating apparatus shown in Figure 6 to assess the model's ability to predict erosion locations. The apparatus comprised a mixing tank, a centrifugal pump, flow meters, regulating valves, and a float-valve test section. The test was performed at a flow rate of 20 L/s and a sand volume fraction of 10% for 10 h. The corresponding simulation used the same flow rate and solid volume fraction.

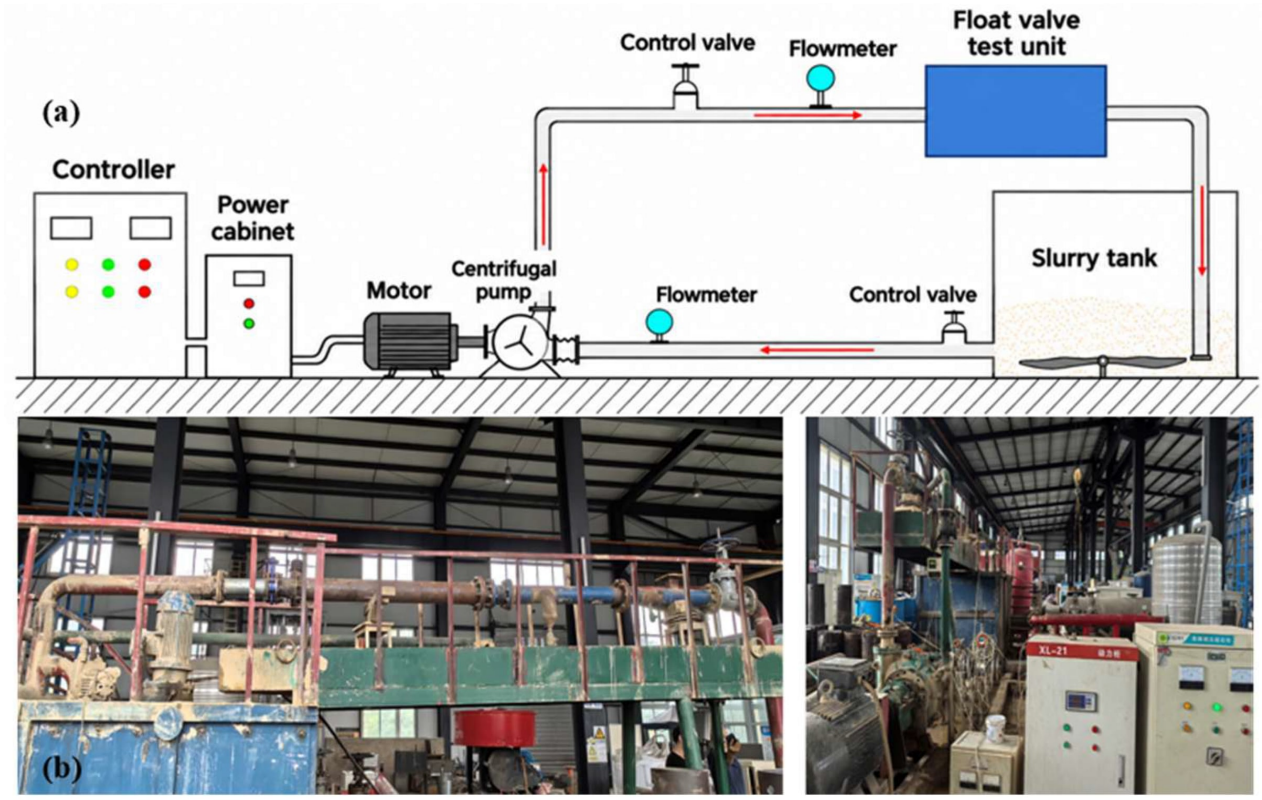


Figure 6. Recirculating apparatus for the erosion test: schematic (**a**) and laboratory setup (**b**).

After the test, the damaged valve cover was examined and compared with the simulated erosion distribution (Figure 7). Both the experiment and simulation showed that the principal erosion region was located at the upper end of the valve cover adjacent to the pin shaft. This spatial agreement supports the model's ability to identify the critical erosion region and provides qualitative validation of the predicted erosion distribution.

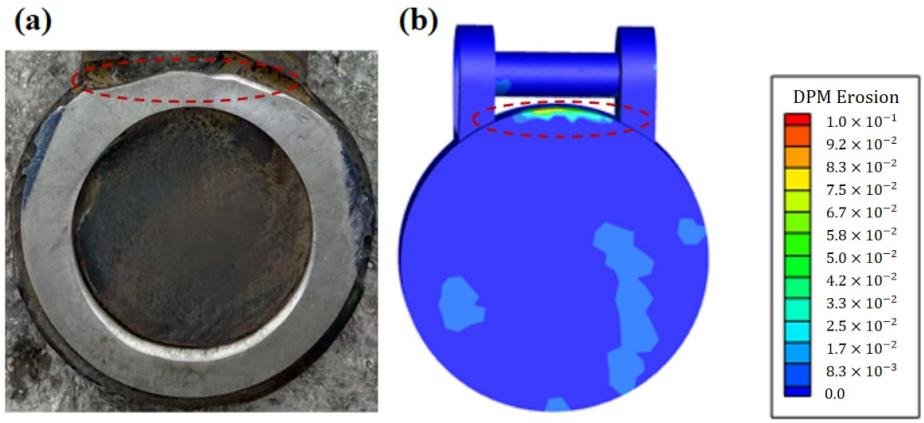


Figure 7. Comparison of erosion on the valve cover: experimental damage after 10 h (**a**) and simulated erosion distribution (**b**).

3. Results and Discussion

3.1. Effect of the Inlet Inclination Angle on the Flow Field and Erosion

To investigate the effect of the inlet inclination angle on the flow field and erosion behavior, simulations were performed for angles from 4.5° to 8.5° at an inlet flow rate of 20 L/s, a solid concentration of 0.5%, and a drilling fluid viscosity of 20 mPa·s. Figure 8 shows the velocity contours in the internal flow field at different inlet inclination angles. As the angle increases from 4.5° to 8.5°, the streamlines inside the spool are significantly deflected. To examine the changes near the valve cover and pin shaft more closely, enlarged flow-field views are presented in Figure 9. At 4.5°, the main drilling fluid jet impinges directly on the top of the valve cover, and strong local vortices and recirculation form near the top of the valve cover and the pin shaft. These flow features can cause solid particles to accumulate and repeatedly impact the wall. At 8.5°, the internal streamlines become smoother and the vortex structures are significantly weakened, reducing the direct impact of the drilling fluid on key regions such as the valve cover and pin shaft.

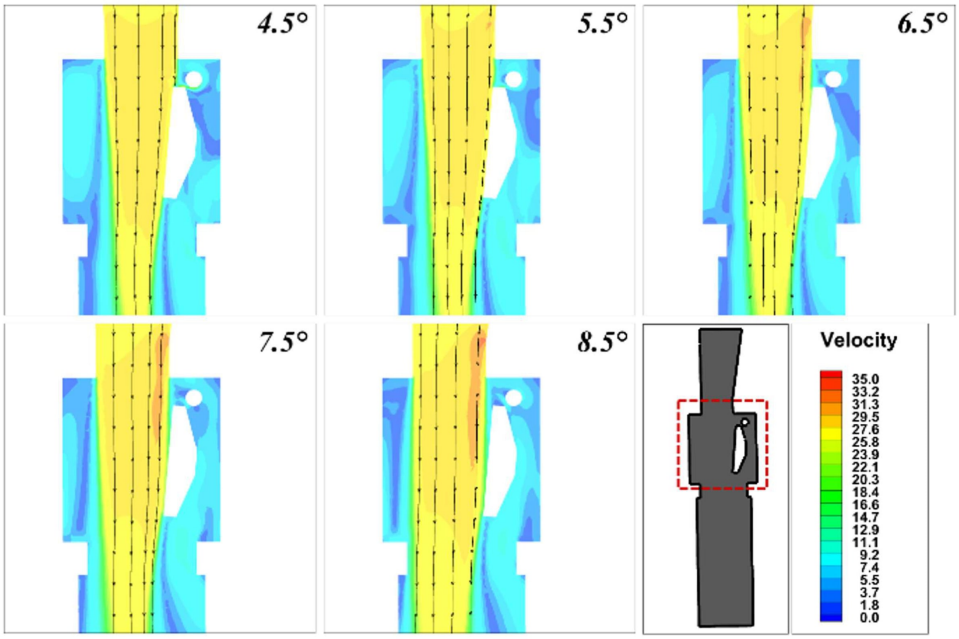


Figure 8. Velocity contours in the internal flow field at different inlet inclination angles.

Figure 10 shows the distribution of the average erosion rate on the valve cover and pin shaft at different inlet inclination angles. At 4.5°, a concentrated high-erosion region appears at the connection between the valve cover and pin shaft, which is a weak point susceptible to erosion failure. As the inclination angle increases, this high-erosion region shifts and diminishes significantly. At 8.5°, severe local erosion on the valve cover is essentially eliminated, and the erosion distribution becomes more uniform. Figure 11 shows the average erosion rates of the valve spool body and valve cover as functions of inlet inclination angle. The average erosion rates decrease substantially with increasing angle. These results indicate that increasing the inlet inclination angle can reduce severe scouring of the valve cover and pin shaft by the drilling fluid and improve the service life of the float valve.

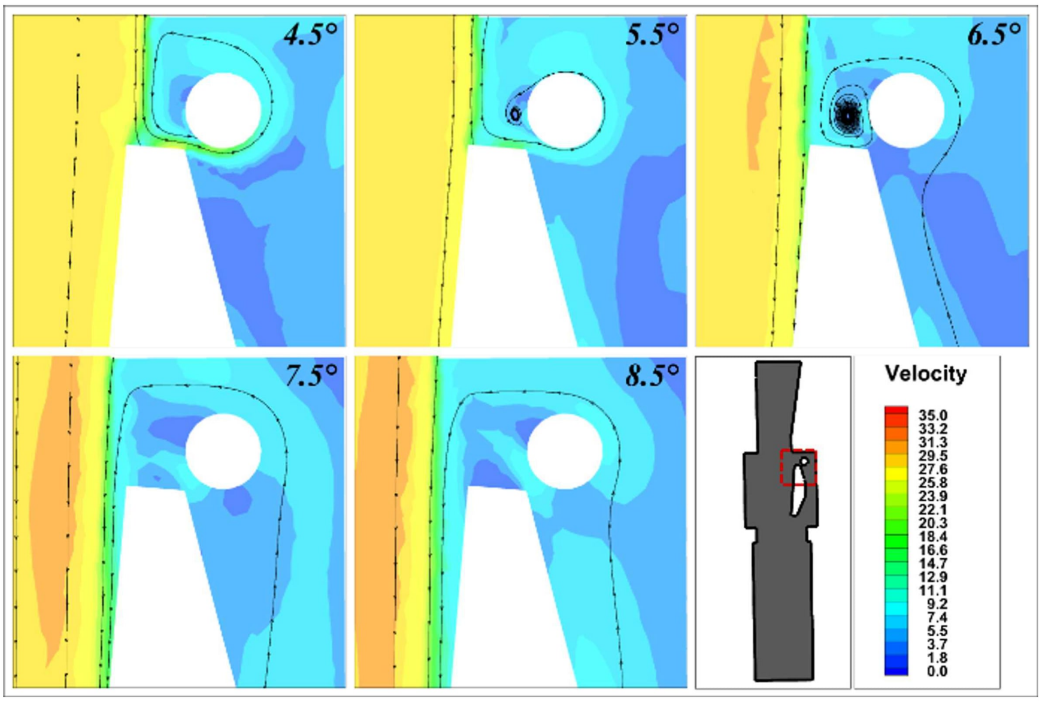


Figure 9. Enlarged velocity contours in the internal flow field at different inlet inclination angles.

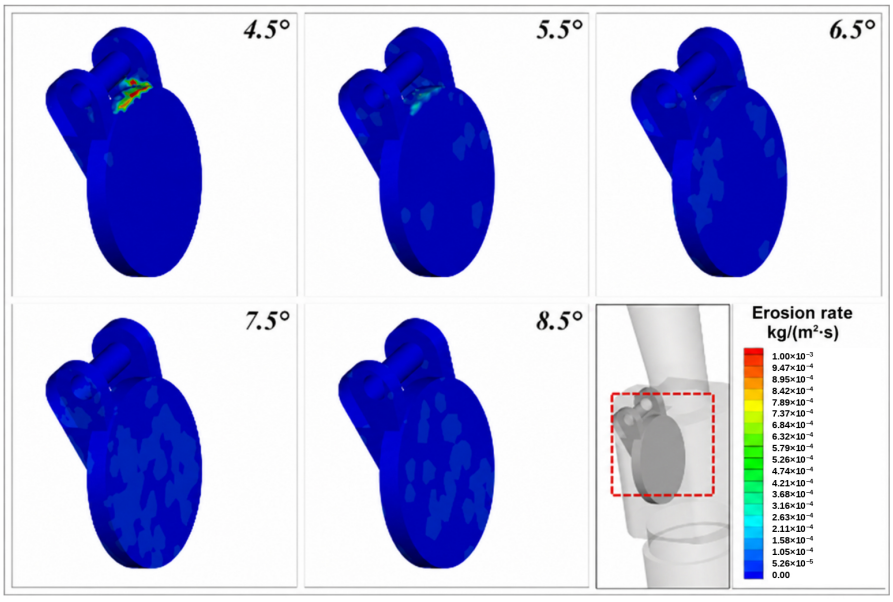


Figure 10. Average erosion-rate contours on the valve cover and pin shaft at different inlet inclination angles.

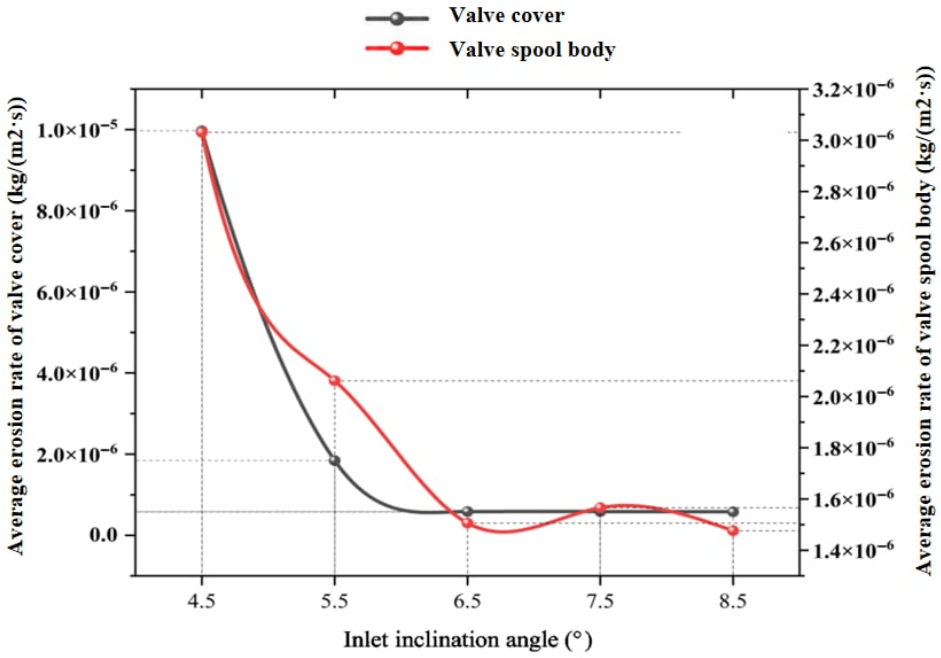


Figure 11. Variation in the average erosion rates of the valve spool body and valve cover with inlet inclination angle.

3.2. Effect of the Inlet Inclination Angle on Erosion with Varying Particle Size

At an inlet flow rate of 20 L/s, a solid concentration of 0.5%, and a drilling fluid viscosity of 20 mPa·s, the effect of particle size (0.106–1.08 mm) on erosion was investigated for different inlet inclination angles. Figures 12 and 13 show the average erosion-rate contours of the valve spool body and valve cover for the original angle (4.5°) at different particle sizes. As shown in Figure 14, the kinetic energy carried by the solid particles increases with particle size, making impact-induced microcutting and fatigue spalling more severe. Consequently, erosion at the inlet contraction of the valve spool body and on the valve cover increases markedly. When the particle size exceeds 0.6 mm, high-erosion patches on the valve cover and pin shaft expand considerably, indicating that the original structure has limited resistance to large particles and is susceptible to local wear failure.

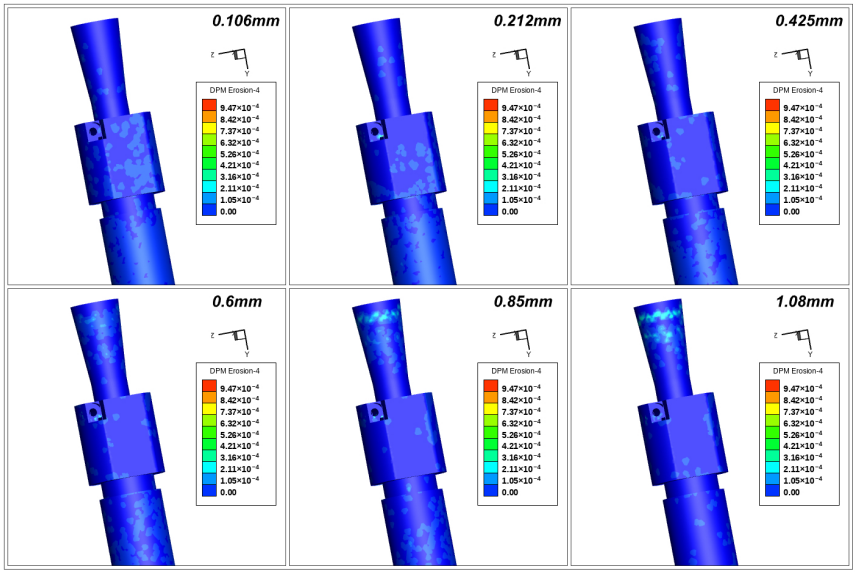


Figure 12. Effect of particle size on the average erosion rate of the valve spool body at the original inclination angle.

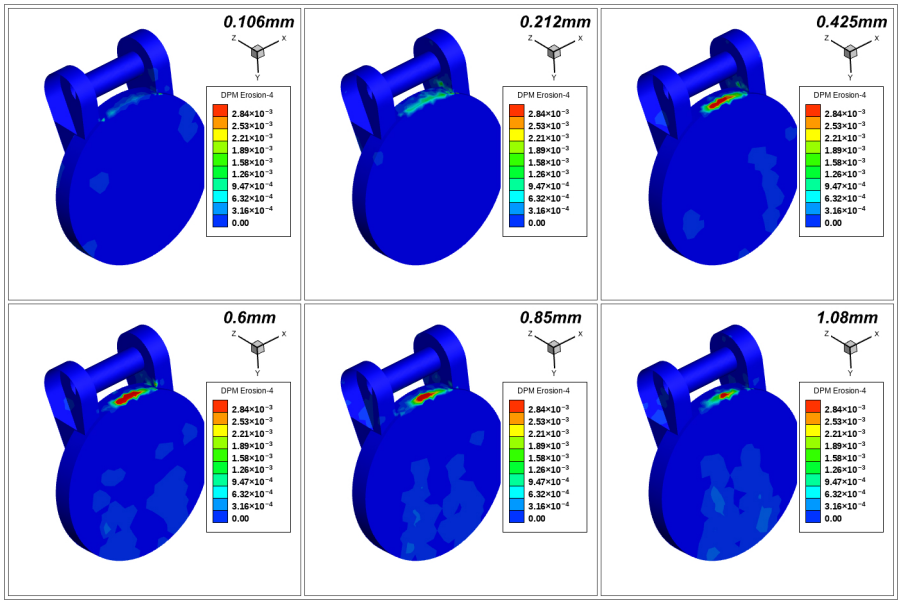


Figure 13. Effect of particle size on the average erosion rate of the valve cover at the original inclination angle.

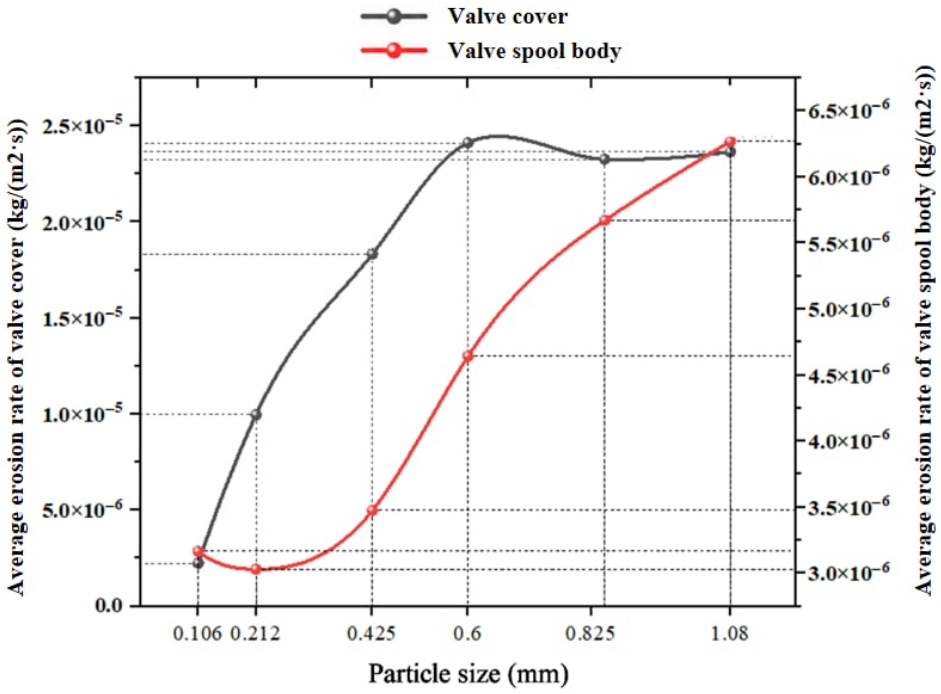


Figure 14. Effect of particle size on the average erosion rates of the valve spool body and valve cover at the original inclination angle.

For the improved angle (8.5°), the average erosion-rate contours of the valve spool body and valve cover at different particle sizes are shown in Figures 15 and 16. As shown in Figure 17, the improved structure exhibits substantially less erosion than the original structure (4.5°) over the studied range. With increasing particle size, valve spool body erosion first decreases and then increases, whereas valve cover erosion decreases. Even for large particles with diameters of 0.85 and 1.08 mm, erosion of the valve cover remains very low. Although large particles still cause some erosion in the contraction section of the valve spool body, the key components (valve cover and pin shaft) experience lower predicted erosion, suggesting a potential service-life benefit. The improved performance is attributed to the change in fluid distribution caused by the inlet inclination angle, which deflects the

flow field. Particle impact then depends on the competing effects of particle inertia and fluid drag. Small particles are dominated by fluid drag and closely follow the flow. Even if the main jet is deflected, these particles are readily entrained by the fluid and move with local detached vortices or recirculation toward the valve cover surface, maintaining a certain erosion rate. Large particles have weaker flow-following ability; as particle size increases, their inertia increases sharply and fluid drag cannot substantially alter their trajectories over short distances. Because the improved inlet angle directs the initial particle path away from the valve cover, large particles can overcome the drag of local vortices and retain their original motion direction.

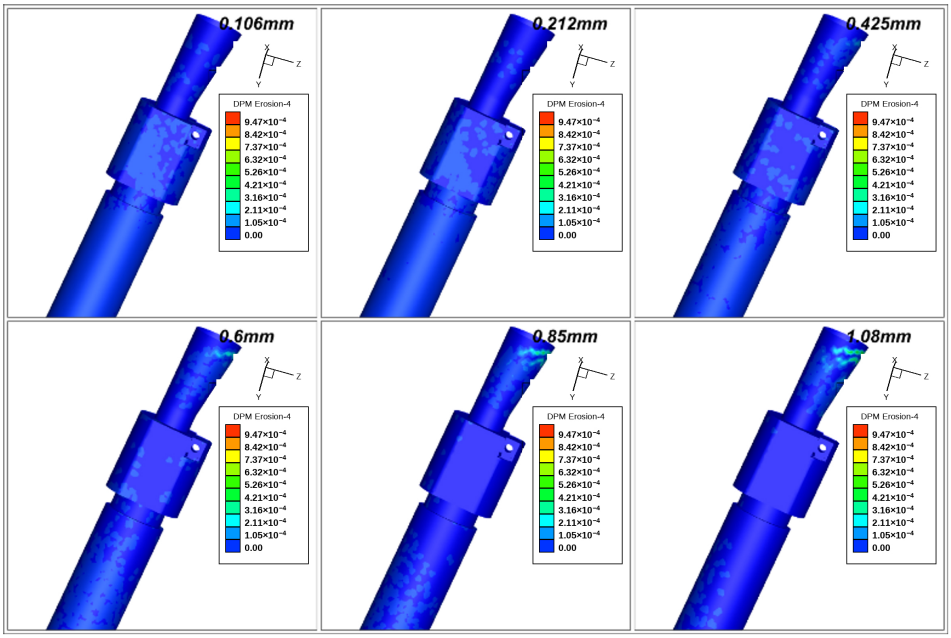


Figure 15. Effect of particle size on the average erosion rate of the valve spool body at the improved inclination angle.

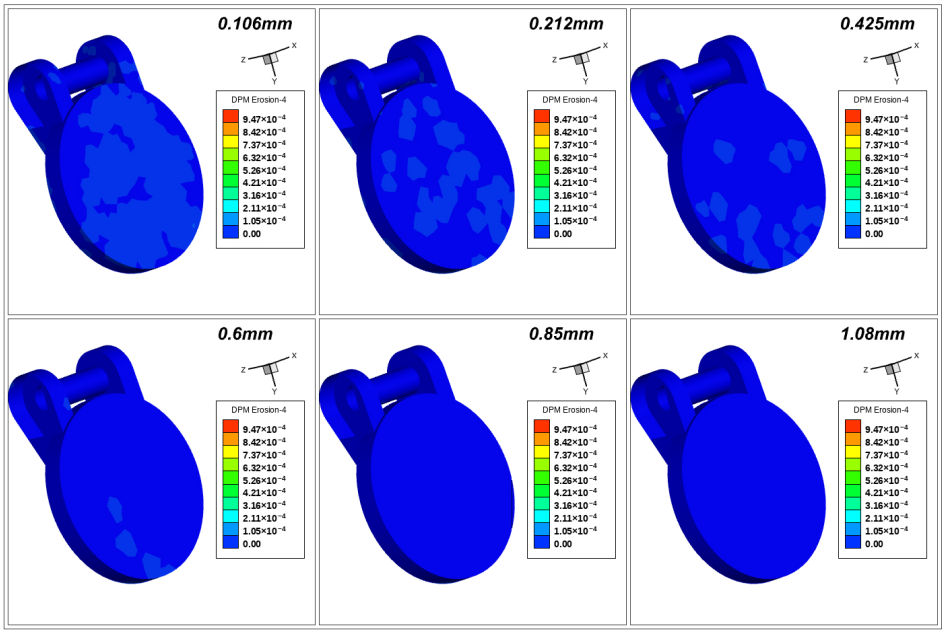


Figure 16. Effect of particle size on the average erosion rate of the valve cover at the improved inclination angle.

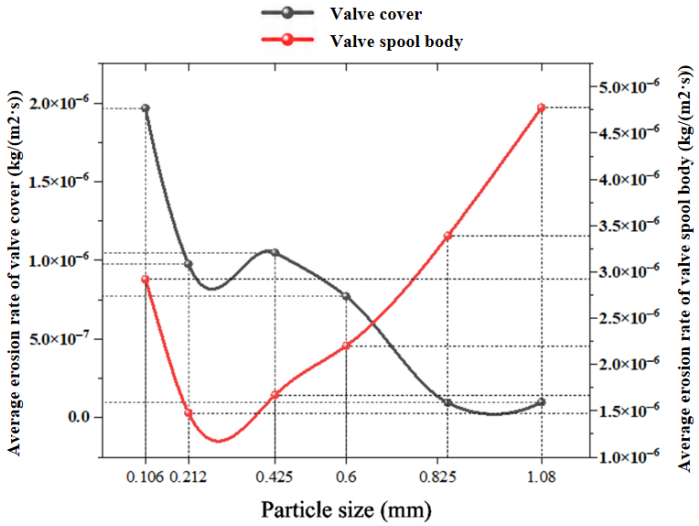


Figure 17. Effect of particle size on the average erosion rates of the valve spool body and valve cover at the improved inclination angle.

3.3. Effect of the Inlet Inclination Angle on Erosion with Varying Drilling Fluid Viscosity

In solid–liquid multiphase flow, fluid viscosity strongly affects particle trajectories and impact kinetic energy. To investigate the influence of drilling fluid viscosity on erosion, simulations were performed at an inlet flow rate of 20 L/s, a solid concentration of 0.5%, and a particle size of 0.212 mm. The erosion behavior of the original and improved structures was evaluated for viscosities from 20 to 100 mPa·s. At 4.5°, the average erosion rates of the valve cover and valve spool body decrease significantly as viscosity increases (Figures 18 and 19). Because the jet directly impacts the valve cover, the erosion rate in this region is relatively high; however, it decreases exponentially as viscosity increases from 20 to 100 mPa·s (Figure 20). At higher viscosity, the viscous shear force increases, the velocity boundary layer near the wall thickens, and the boundary layer buffers particle motion. As particles pass through this high-viscosity layer, they experience strong fluid drag, decelerate sharply, and lose much of their impact kinetic energy. Consequently, the macroscopic erosion rate decreases with increasing viscosity.

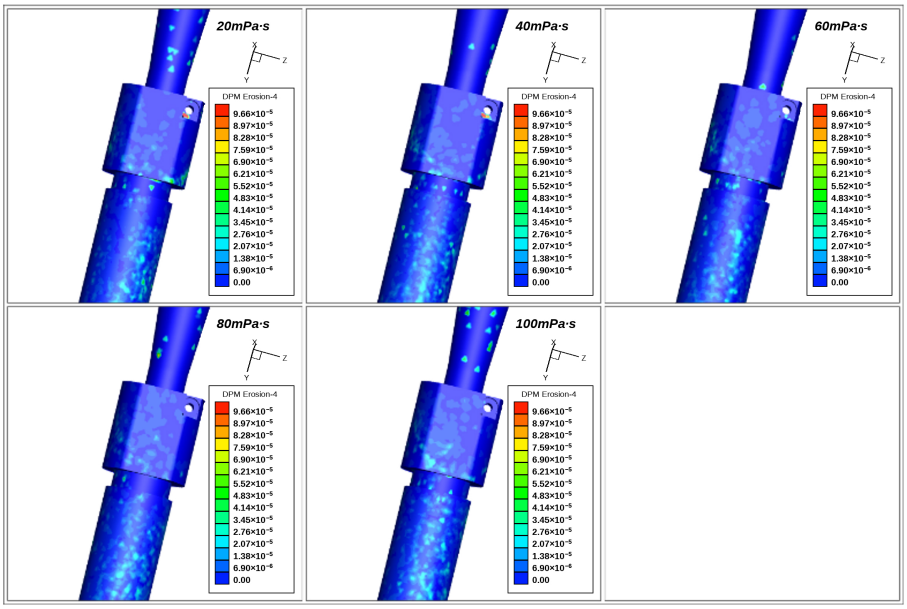


Figure 18. Effect of drilling fluid viscosity on the average erosion rate of the valve spool body at the original inclination angle.

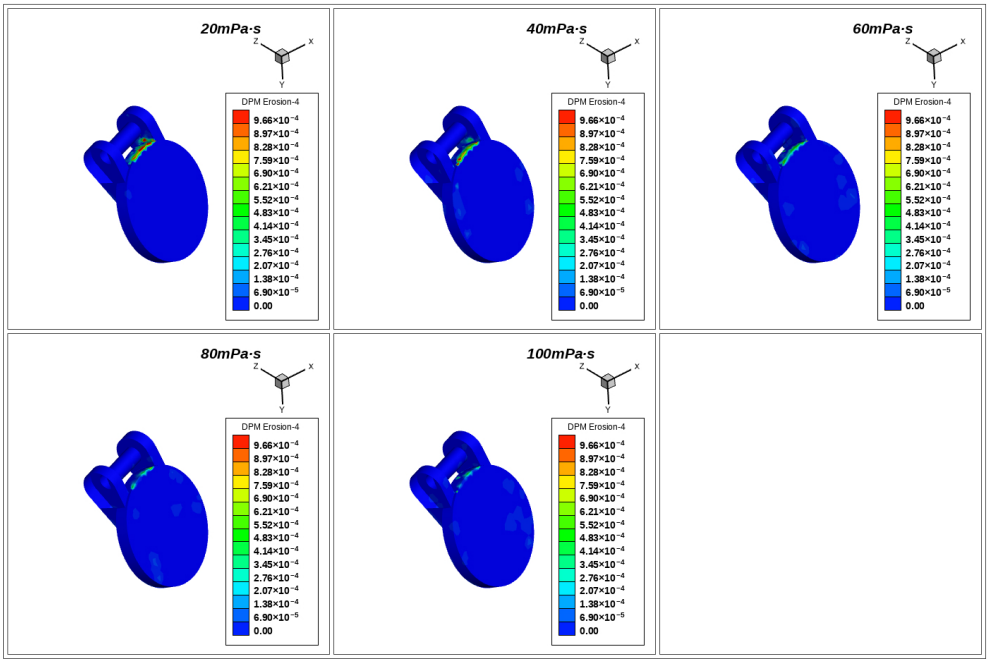


Figure 19. Effect of drilling fluid viscosity on the average erosion rate of the valve cover at the original inclination angle.

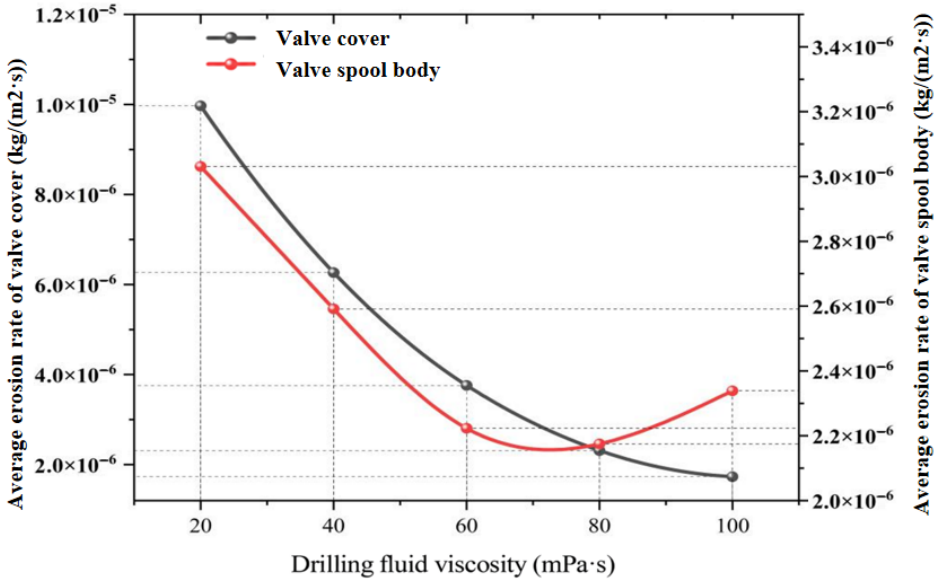


Figure 20. Effect of drilling fluid viscosity on the average erosion rates of the valve spool body and valve cover at the original inclination angle.

Figures 21–23 show that, for the improved structure (inlet inclination angle of 8.5°), the erosion-rate curves for the valve spool body and valve cover fluctuate as the drilling fluid viscosity varies. Compared with the original structure, the average erosion rate of the improved structure remains about one order of magnitude lower. This behavior occurs because changes in viscosity alter the drag force on the particles and the local turbulence, causing fluctuations in impact angle and impact velocity that produce small increases or decreases in the already low erosion at different locations.

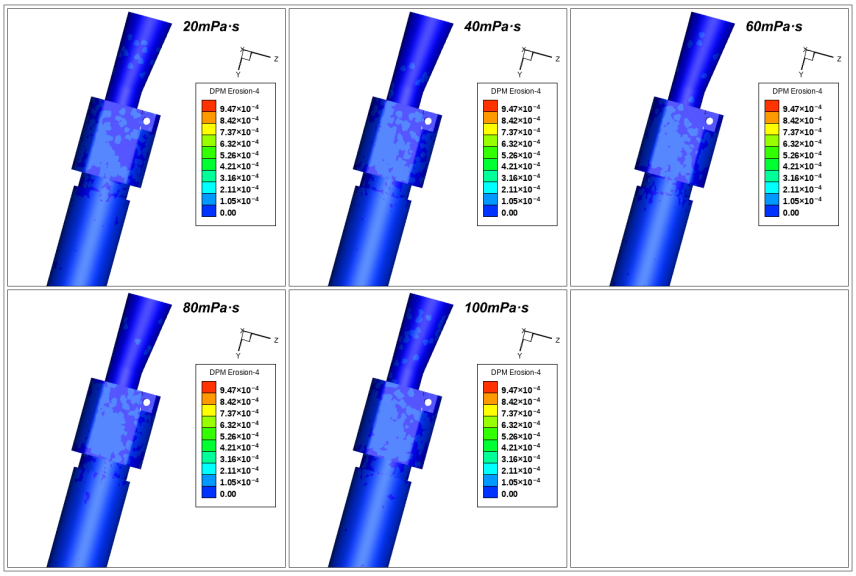


Figure 21. Effect of drilling fluid viscosity on the average erosion rate of the valve spool body at the improved inclination angle.

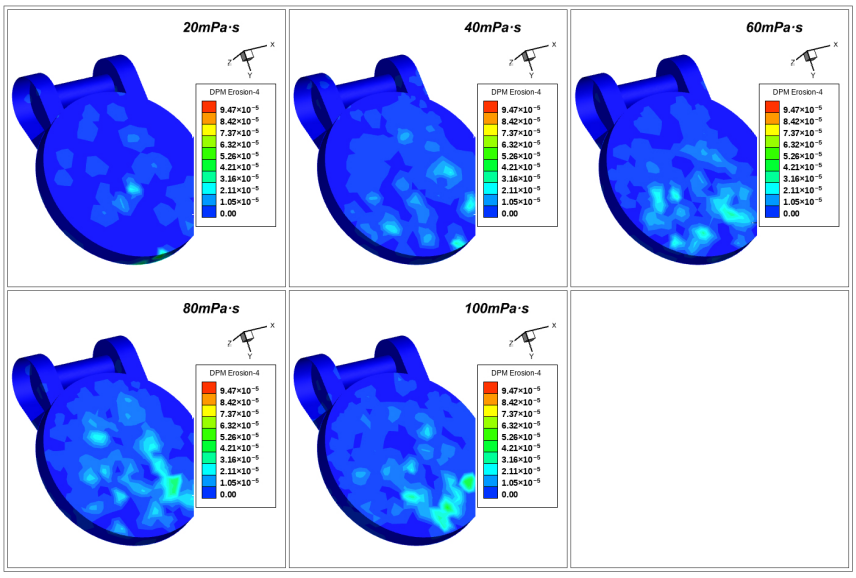


Figure 22. Effect of drilling fluid viscosity on the average erosion rate of the valve cover at the improved inclination angle.

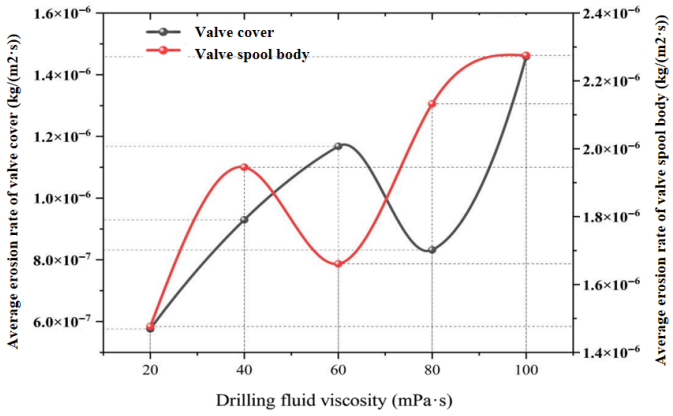


Figure 23. Effect of drilling fluid viscosity on the average erosion rates of the valve spool body and valve cover at the improved inclination angle.

3.4. Effect of the Inlet Inclination Angle on Erosion with Varying Solid Concentration

Solid concentration directly controls the number of particles that impact the wall per unit time and is a key indicator of the tolerance of the float valve under harsh conditions. To investigate the effect of solid concentration on erosion, simulations were performed at an inlet flow rate of 20 L/s, a drilling fluid viscosity of 20 mPa·s, and a particle size of 0.212 mm for solid concentrations from 0.5% to 2.5%. As shown in Figures 24 and 25, both the original and improved structures exhibit similar trends: the average erosion rates of the valve spool body and valve cover increase linearly with solid concentration. Under the adopted one-way-coupled DPM approximation, particles are tracked independently, with particle-particle collisions neglected. Therefore, as the concentration increases linearly from 0.5% to 2.5%, the number of particles impacting the wall per unit time increases proportionally. Although both structures exhibit linear behavior with respect to concentration, their erosion rates and erosion regions differ significantly.

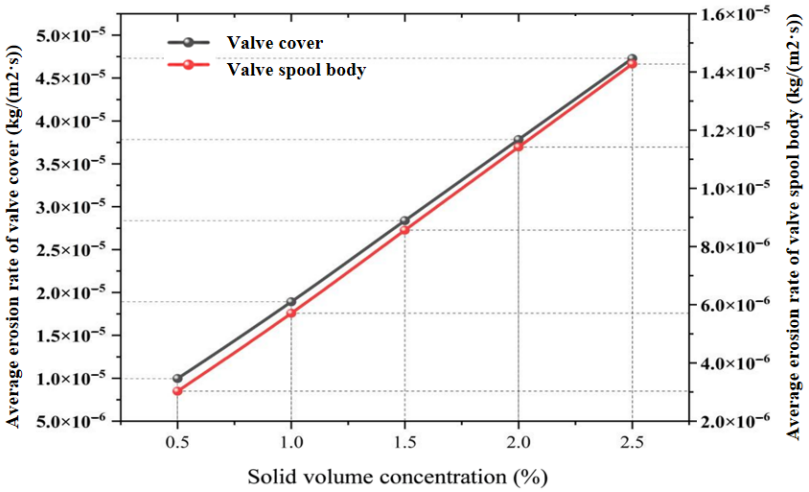


Figure 24. Effect of solid concentration on the average erosion rates of the valve spool body and valve cover at the original inlet inclination angle.

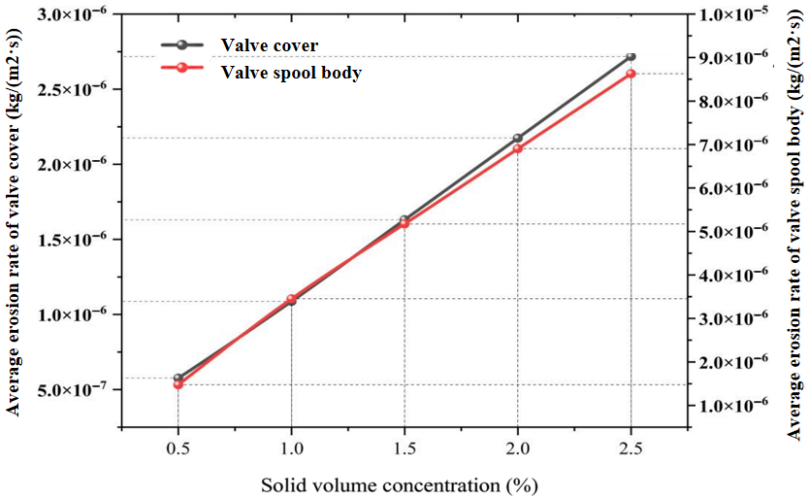


Figure 25. Effect of solid concentration on the average erosion rates of the valve spool body and valve cover at the improved inlet inclination angle.

A comparison of the erosion contours on the valve cover before and after optimization shows that (Figures 26 and 27), in the original structure, the red high-erosion region around the valve cover pin shaft expands rapidly as solid concentration increases, making localized

perforation or fracture likely. In the improved structure, the key valve cover region still exhibits a low erosion rate even when the solid concentration reaches 2.5%. Although the eccentric flow passage of the improved float valve cannot change the general rule that more particles cause more erosion, it reduces the average erosion rate by altering the flow-field distribution.

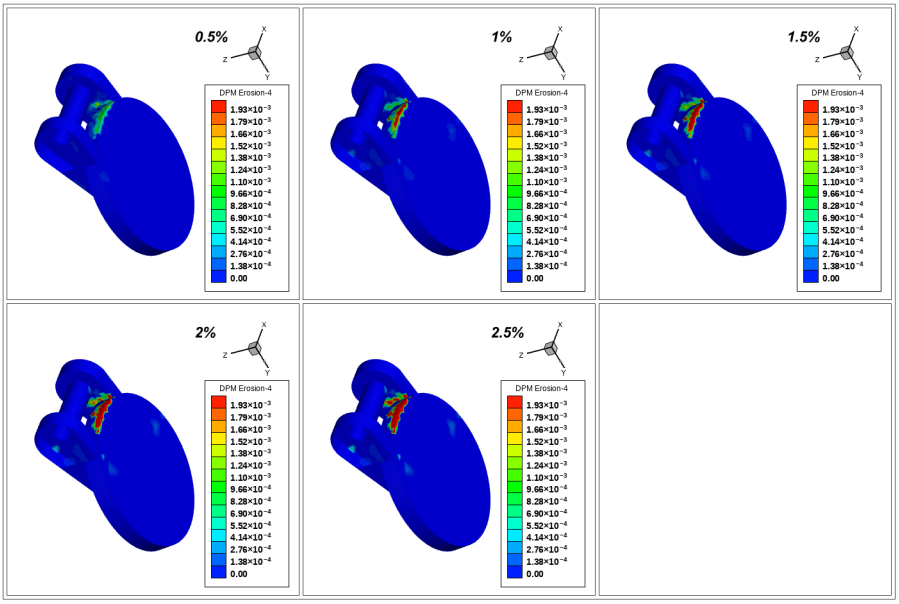


Figure 26. Effect of solid concentration on the average erosion rate of the valve cover at the original inlet inclination angle.

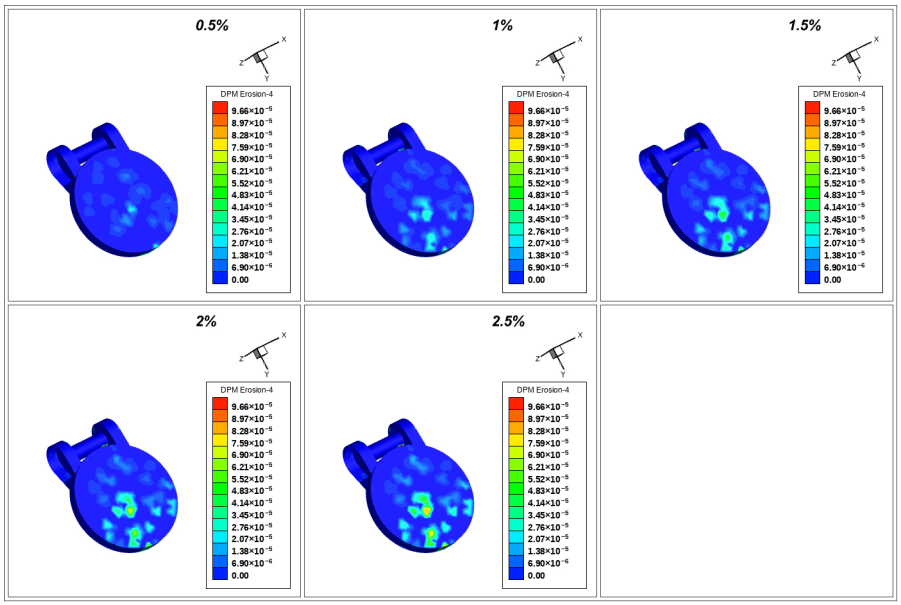


Figure 27. Effect of solid concentration on the average erosion rate of the valve cover at the improved inlet inclination angle.

4. Conclusions

This study investigated the influence of the inlet inclination angle on the erosion characteristics of a drilling float valve and analyzed the erosion behavior for different particle sizes, drilling fluid viscosities, and solid concentrations before and after optimization. The main conclusions are as follows:

(1) The inlet inclination angle is a key geometric parameter affecting the internal flow-field distribution and erosion behavior of the float valve. When the inclination angle increases from 4.5° to 8.5°, the main flow inside the spool is significantly deflected, and strong vortices and recirculation in the valve cover and pin shaft regions are substantially weakened. The concentrated high-erosion zones shift and diminish, the average erosion rates of the valve spool body and valve cover decrease markedly, and the erosion distribution becomes more uniform.

(2) Particle size has a non-monotonic effect on float valve erosion. For the original structure (4.5°), particles with diameters of 0.6 mm or larger rapidly expand erosion patches on the valve cover and pin shaft. In the improved structure (8.5°), the eccentric flow passage changes the initial particle incidence direction. Large particles bypass the valve cover region because of their high inertia, while small particles remain more flow-following because of fluid drag. The improved structure significantly reduces the erosion risk of key components under all investigated particle sizes.

(3) Increasing drilling fluid viscosity reduces erosion. For the original structure, increasing the viscosity from 20 to 100 mPa·s decreases valve cover erosion exponentially. This reduction is attributed to the buffering effect of the high-viscosity boundary layer near the wall, which consumes particle impact kinetic energy. The improved structure maintains an average erosion rate well below that of the original structure under various viscosities.

(4) Erosion rate increases linearly with solid concentration for both structures. The improved structure does not change this linear relationship, but it reduces the overall erosion level by about one order of magnitude through flow-field optimization. Even at a solid concentration of 2.5%, the key valve cover region exhibits a very low erosion rate, indicating that the improved structure has greater tolerance to high-sand-content conditions.

(5) Engineering implications. Increasing the inlet inclination angle to 8.5° redirects the particle-laden flow away from the valve cover and pin shaft, reducing erosion of these critical components. The comparative tests showed visibly less valve-cover damage for the modified configuration after 15 h, qualitatively supporting the predicted improvement. This modification provides a practical approach to improving the erosion resistance of the investigated float valve.

(6) Limitations. The recommended angle of 8.5° applies to the investigated geometry and seal-installation constraints and should not be regarded as a universal optimum.

Author Contributions: Methodology, X.Z. (Xin Zhang) and J.L.; Software, L.Z.; Validation, Y.L. and L.Z.; Writing—original draft preparation, X.Z. (Xin Zhang) and L.Z.; Writing—review and editing, Y.L., X.S. and X.Z. (Xuliang Zhang). All authors have read and agreed to the published version of the manuscript.

Funding: This research was funded by the Scientific Research Project of Tarim Oilfield Company, grant number T202508 and the Sichuan Association for Science and Technology, grant number 2023NSFSC1980.

Data Availability Statement: The original contributions presented in this study are included in the article. Further inquiries can be directed to the corresponding authors.

Conflicts of Interest: Author Xin Zhang, Junan Lu, Yanwen Liu, Xitian Shi, and Xuliang Zhang are now employed by the Petrochina Tarim Oilfield Company. The remaining author declares that the research was conducted in the absence of any commercial or financial relationships that could be construed as potential conflicts of interest.

Abbreviations

The following abbreviations are used in this manuscript:

CFD	Computational fluid dynamics
HBW	Brinell hardness
HV	Vickers hardness

References

1. Jiang, G.; Lin, F.; Jia, H. Well Control Safety Strategy for High-Sulfur Areas of the Tarim Oilfield. *Neijiang Sci. Technol.* **2022**, *43*, 14–15.
2. Jiang, G.; Lin, F.; Jia, H. Analysis and Research on Well Control Technology for Exploration Wells in the Tarim Oilfield. *Neijiang Sci. Technol.* **2022**, *43*, 73–74.
3. Yu, J.; Wang, C. Tarim Oilfield Drills 250 "Underground Everest" Wells. *Tianshan Net-Xinjiang Daily*, 2 February 2026.
4. Niu, X.; Zhang, J.; Zhou, H. Technical Difficulties and Countermeasures for Well Control in "Three-Super" Oil and Gas Wells. *Pet. Drill. Tech.* **2017**, *45*, 1–7.
5. Zhu, X. Research and Prospects for Rate of Penetration Improvement in Deep and Ultra-Deep Oil and Gas Drilling. *J. Southwest Pet. Univ. (Sci. Technol. Ed.)* **2025**, *47*, 1–9.
6. Wang, K.; Zhang, X. A Reliability Analysis of IBOPs in Nitrogen Drilling of Tarim Oilfield. *Ind. Eng. J.* **2015**, *18*, 151–159.
7. Xiao, L.; Zheng, Y.; Zheng, J.; Liu, M.; Xie, Y. Development and Application of the "F" Type Drill Pipe Float Valve. *Drill. Prod. Technol.* **2010**, *33*, 80–82.
8. Gao, C.; Zheng, J.; Jing, Y.; Li, Z.; Li, H.; Cai, L. Development and Application of Full Diameter Inside Blowout Preventer. *Drill. Prod. Technol.* **2011**, *34*, 65–67.
9. Chen, H.; Wang, C.; Wu, Z.; Pei, Y.; Su, Y. Working Mechanism and Failure Analysis of Check Valves of BOP (Blowout Preventer) System in Drilling String for Safe Drilling. *Nat. Gas. Ind.* **2010**, *30*, 69–72.
10. Zhang, X.; Wang, Q.; Yan, Y.; Tao, Y.; Cai, G.; Yang, W. Simulation Analysis of Flow Field of the Flapper Float Valve Based on CFD. *Oil Field Equip.* **2015**, *44*, 22–26.
11. Xu, Y.; Guan, Z.; Liu, Y.; Xuan, L.; Zhang, H.; Xu, C. Structural Optimization of Downhole Float Valve via Computational Fluid Dynamics. *Eng. Fail. Anal.* **2014**, *44*, 85–94. [CrossRef]
12. Tang, Y.; Zhao, P.; Fang, X.; Wang, G.; Zhong, L.; Li, X. Numerical Simulation on Erosion Wear Law of Pressure-Controlled Injection Tool in Solid Fluidization Exploitation of the Deep-Water Natural Gas Hydrate. *Energies* **2022**, *15*, 5314. [CrossRef]
13. Zhang, Y.; Zhang, L.; Gao, Y.; Shi, P.; Wang, Y.; Kong, L. Research on Erosion Damage Laws and Structural Optimization of Bypass Valve for Positive Displacement Motors. *Processes* **2024**, *12*, 1953. [CrossRef]
14. Zhao, Z.; Wu, Z.; Wang, W.; Wang, X.; Du, S.; Chen, X.; Li, P.; Wang, Y. CFD-DPM Model of Gas–Solid Two-Phase Flow Erosion of Needle Throttle Valve. *Coatings* **2025**, *15*, 248. [CrossRef]
15. Wang, Y.; Kong, W.; Li, J.; Sun, H.; Li, X.; Wei, Q. A Decoupling Model for Fatigue Life Assessment of Double Wellhead System with Subsea Suction Anchor. *Ocean Eng.* **2024**, *311*, 118896. [CrossRef]
16. Wang, Q.; Xu, Z.; Jia, W.; Song, X.; Li, G.; Zhou, M.; Qu, H.; Huang, S.; Gou, T.; Yuan, Z. Active Wellbore Cooling during Deep Drilling Circulation via Microencapsulated Phase Change Materials: Energy Redistribution Mechanism and Inverse Design. *Energy* **2026**, *360*, 141647. [CrossRef]
17. Bi, G.; Wang, X.; Li, M.; Wu, J.; Han, F.; Yuan, P.; Fu, S. Structural Design and Flow Field Characteristics Analysis of a New Spin-on Multi-Hole Jet Drill Bit for Radial Horizontal Wells. *Geoenergy Sci. Eng.* **2023**, *230*, 212173. [CrossRef]
18. Yang, Y.; Li, Q.; Xu, Y.; Huang, J. Dynamics Study of Self-Pulling & Self-Rotating Jet Drill Bit in Natural Gas Hydrate Reservoirs Radial Horizontal Well Drilling. *Geoenergy Sci. Eng.* **2025**, *244*, 213490. [CrossRef]
19. Oka, Y.I.; Yoshida, T. Practical estimation of erosion damage caused by solid particle impact. Part 2: Mechanical properties of materials directly associated with erosion damage. *Wear* **2005**, *259*, 102–109. [CrossRef]

Disclaimer/Publisher's Note: The statements, opinions and data contained in all publications are solely those of the individual author(s) and contributor(s) and not of MDPI and/or the editor(s). MDPI and/or the editor(s) disclaim responsibility for any injury to people or property resulting from any ideas, methods, instructions or products referred to in the content.